

Cite this: *Nanoscale*, 2019, **11**, 17368

## The device level modulation of carrier transport in a 2D WSe<sub>2</sub> field effect transistor via a plasma treatment†

Inyong Moon,<sup>‡,a</sup> Sungwon Lee,<sup>‡,a</sup> Myeongjin Lee,<sup>a</sup> Changsik Kim,<sup>a</sup> Daehee Seol,<sup>b</sup> Yunseok Kim,<sup>ID, b</sup> Ki Hyun Kim,<sup>b</sup> Geun Young Yeom,<sup>ID, a,b</sup> James T. Teherani,<sup>c</sup> James Hone<sup>d</sup> and Won Jong Yoo <sup>ID, \*a</sup>

Tungsten diselenide (WSe<sub>2</sub>) has received significant attention because it shows the pristine ambipolar property arising from the Fermi level located near the midgap and can be converted to uni-polar form. In this study, we observe the formation of tungsten oxide (WO<sub>x</sub>) on the WSe<sub>2</sub> surface after oxygen plasma treatment and show that the p-type WO<sub>x</sub> dopes WSe<sub>2</sub>. In our devices that underwent plasma treatment, it was interesting to find a strong correlation between the changes in the work function of WSe<sub>2</sub> and a gold electrode, and the channel and contact resistances. The channel resistance changes very sensitively at a rate of 64 meV per dec with the increase in the WSe<sub>2</sub> channel work function, which is close to the thermal limit; this indicates the defect-free oxidized WSe<sub>2</sub> channel. The carrier transport in the oxidized WSe<sub>2</sub> FET is shown to change to a high performance p-type device with greatly reduced channel and contact resistances with the increase in the plasma oxidation time.

Received 11th July 2019,  
Accepted 28th August 2019  
DOI: 10.1039/c9nr05881h  
[rsc.li/nanoscale](http://rsc.li/nanoscale)

### 1. Introduction

Two dimensional (2D) materials have great potential for use as next-generation semiconductors because they have tunable band gaps, high mobility channels, and high conductivity despite their ultra-thin width of a few nanometers.<sup>1,2</sup> Particularly, among the 2D materials, transition metal dichalcogenides (TMDCs) are considered as leading candidates that can supplement the fast pace of innovations that was previously led by silicon. As a TMDC, monolayer tungsten diselenide (WSe<sub>2</sub>) has a band gap of 1.6 eV and little band gap fluctuation is observed as the WSe<sub>2</sub> thickness becomes large (1.2 eV).<sup>3</sup> In its pristine state, WSe<sub>2</sub> has been measured to have a room-temperature mobility of 250 cm<sup>2</sup> V<sup>-1</sup> s<sup>-1</sup>, an on/off ratio of 10<sup>6</sup>, and a subthreshold swing of 60 mV per decade.<sup>4</sup>

Since the pristine Fermi level is located near the midgap, it is more facile to dope a pristine sample to make it n-type or p-type<sup>5–7</sup> than other contending 2D materials, which is advantageous for the formation of pn junction as the key building block required in most semiconductor device structures. In particular, tungsten oxide (WO<sub>x</sub>) formed from the oxidation of WSe<sub>2</sub> has a very high work function and can be used as a p-type dopant in devices such as OLEDs.<sup>6</sup> The research on using WO<sub>x</sub> as a p-type dopant in WSe<sub>2</sub> field-effect transistors has been recently pursued.<sup>5,6,9,10</sup>

Previous research on oxidized WSe<sub>2</sub> FETs has focused on studying the oxidation of WSe<sub>2</sub> as the channel material but was inobservant to the changes in properties due to oxidation of the metal electrodes. However, a study by Hou *et al.*<sup>11</sup> showed that the work function increases by up to 0.5–0.8 eV when metals with high work function (such as gold, palladium, and platinum) are oxidized. The work function increase in the metals due to oxidation has also been studied in fields requiring precise band alignment, such as organic electronics and power electronics.<sup>11–14</sup>

The work function of various 2D materials is a critically important parameter to explore their device characteristics, requiring the development of reliable work function measurement techniques for ultrathin 2D materials. It is known that UPS is similar in principle to XPS, except that the radiation source is an ultraviolet light (~20 eV) instead of X-rays (~1250 eV), enabling the effective measurement of the work

<sup>a</sup>SKKU Advanced Institute of Nano-Technology (SAINT), Sungkyunkwan University, 2066, Seobu-ro, Jangan-gu, Suwon, Gyeonggi-do, 16419, Korea.

E-mail: [yoowj@skku.edu](mailto:yoowj@skku.edu)

<sup>b</sup>School of Advanced Materials Science and Engineering, Sungkyunkwan University, 2066 Seobu-ro, Jangan-gu, Suwon, Gyeonggi-do, 16419 Korea

<sup>c</sup>Department of Electrical Engineering, Columbia University, New York, NY 10027, USA

<sup>d</sup>Department of Mechanical Engineering, Columbia University, New York, NY 10027, USA

† Electronic supplementary information (ESI) available. See DOI: [10.1039/c9nr05881h](https://doi.org/10.1039/c9nr05881h)

‡ I. Moon and S. Lee contributed equally to this work.

function of semiconductor materials.<sup>15,16</sup> However, a sample size of at least a few hundred micrometers and an ultra-high vacuum environment are necessary to avoid high noise levels due to the limits in focusing the UV light source, thus limiting its application to the study of small-sized 2D materials at the device level. In contrast, the Kelvin probe force microscopy (KPFM), as a technique capable of measuring the contact potential difference ( $V_{CPD}$ ) between the sample surface and a metal tip, is held several tens of nanometers above the sample surface,<sup>17–19</sup> thus enabling the analysis of surface sensitive small-sized 2D materials at the device level. The operating principle of KPFM is shown in Fig. S1.† The measured  $V_{CPD}$  value can give the work function of the sample ( $\phi_{sample}$ ) if the work function of the metal tip ( $\phi_{tip}$ ) is known, according to the equation  $eV_{CPD} = \phi_{tip} - \phi_{sample}$ .

In this study, we measure the work function changes in both the WSe<sub>2</sub> channel and gold electrodes at the device level using a non-destructive KPFM technique upon consecutive oxygen plasma treatments and electrically investigate the impact of the plasma treatment on the carrier transport in oxidized WSe<sub>2</sub> FETs by analyzing the current–voltage ( $I$ – $V$ ) characteristics as well as the channel and contact resistances. Furthermore, we wish to propose a correlation between the work function changes in the oxidized WSe<sub>2</sub> channel and the metal electrodes, and the channel and contact resistances.

## 2. Results and discussion

### Chemical composition of the oxidized WSe<sub>2</sub> FET

Fig. 1a shows the cross sectional schematic of the post-oxygen plasma-treated WSe<sub>2</sub> FET used in this study. The pristine WSe<sub>2</sub> device was fabricated by exfoliating WSe<sub>2</sub> on a 285 nm SiO<sub>2</sub> substrate by the scotch tape method. We chose multilayer WSe<sub>2</sub> (~7 to 10 nm thick) to form the FETs. The electrodes were formed by electron beam lithographic patterning and subsequent electron-beam deposition of 50 nm of high purity gold in a high-vacuum environment. The subsequent plasma oxidation of the device generated WO<sub>x</sub> and AuO<sub>x</sub> on the WSe<sub>2</sub> and Au surfaces, respectively.

In Fig. 1b, the position of the W and Se peaks were measured as a function of oxidation time using XPS. The exfoliated WSe<sub>2</sub> samples used for the XPS measurements were prepared on the SiO<sub>2</sub> substrate without Au electrodes. In the pristine state, the W 4f<sub>5/2</sub> and W 4f<sub>7/2</sub> peaks were at 30.9 and 32.9 eV, respectively, and the Se 3d<sub>5/2</sub> and Se 3d<sub>7/2</sub> peaks were at 53.2 and 53.9 eV, respectively. These values match with the previously published data for WSe<sub>2</sub>.<sup>8</sup> The same sample was repeatedly oxidized with oxygen plasma, and then measured at cumulative plasma durations of 4, 20, 84, and 340 seconds. After the initial 4 seconds oxidation, two new peaks appear in the XPS spectrum at the binding energies of 34 and 36.1 eV, which correspond to the reported values for WO<sub>x</sub>.<sup>7,9,10</sup>

WO<sub>x</sub> acts as a strong hole injection material and is known to act as a p-type doping layer for WSe<sub>2</sub>,<sup>9,10,20</sup> we highlight the doping effect by WO<sub>x</sub> through the peak shifts of W 4f and Se

3d, as shown in Fig. 1c, as a function of oxidation time. Overall, the binding energy of the 4f and 3d peaks decrease by 0.4 to 0.6 eV. As the XPS binding energy represents the energy difference between the (doping-dependent) Fermi level and the fixed core level, a decrease in the binding energy suggests that the Fermi level has shifted towards the valence band, indicating that p-type doping has occurred.<sup>10</sup> This p-type doping effect was saturated after 20 seconds of plasma treatment, which can be seen from the peak shifts of W and Se peak that are stagnant after the 20 seconds treatment. The XPS peak of O 1s is shown in Fig. S2.† Like the W and Se peaks, the O peak intensity appears to saturate after 20 seconds. Because the XPS sample was prepared on the silicon oxide substrate, it is reasonable to observe the O 1s peak in the pristine state.

The distribution of WO<sub>x</sub> along the depth direction was analyzed by the time of flight secondary ion mass spectroscopy (TOF SIMS) after the sample had been exposed to 340 seconds of plasma oxidation, as shown in Fig. 1d. Compared to the bulk of the sample, the Se ion intensity peak decreases within the top 1 nm of the structure but the WO<sub>2</sub><sup>−</sup> and the WO<sub>3</sub><sup>−</sup> ion intensity peaks at the surface of the device increase, indicating that a thin layer of WO<sub>x</sub> (with an approximate thickness of 1 nm) was formed at the surface of multilayer WSe<sub>2</sub>. The SIESTA method simulations of stoichiometric WO<sub>x</sub> have reported that WO<sub>3</sub> is an insulator, while WO<sub>2</sub> is a conductor.<sup>21,22</sup> The results of SIMS suggest that the composition of WO<sub>3</sub> is about 10× higher than that of WO<sub>2</sub> for WO<sub>x</sub> formed by our oxygen plasma treatment. A separate experiment testing the plasma oxidation of the monolayer WSe<sub>2</sub> further suggests that our WO<sub>x</sub> is insulating as the on-current of the monolayer WSe<sub>2</sub> p-FET drops to the noise floor of our measurement setup (~1 pA) after 20 seconds of oxidation (see Fig. S3†). TOF SIMS was also performed to confirm the oxidation of the gold surface during plasma oxidation. The fast sputtering rate of gold by Cs<sup>+</sup> ions was 20 times faster than that of WSe<sub>2</sub>, so a precise depth profile was not possible. Nonetheless, the results show the presence of AuO<sub>2</sub> on the electrode surface, as seen in Fig. S4.†

We performed further analysis of the gold surface SIMS profiling. Fig. S5† shows the results of gold oxide (AuO<sub>x</sub>) ion intensity as a function of the oxidation time. A detailed description of the SIMS surface profiling is provided in the Experimental section. The ion intensities of Au<sup>−</sup>, Au<sub>2</sub><sup>−</sup>, AuO<sub>2</sub><sup>−</sup>, and Au<sub>2</sub>O<sub>3</sub><sup>−</sup> were measured. Comparing the results of the pristine sample to the same sample after 340 seconds of plasma treatment, the gold ion intensities decrease about 3 to 10× but the gold oxide ion intensities increase by about 20 to 30×. Previous experiments have suggested that the most stable bonding configuration for gold oxide is Au<sub>2</sub>O<sub>3</sub>.<sup>11</sup> In our results, Au<sub>2</sub>O<sub>3</sub><sup>−</sup> is comparatively absent for the sample in the pristine state but its intensity rapidly increases by up to 100× as the plasma oxidation time is increased. The same trend was also observed for AuO<sub>2</sub><sup>−</sup>. For completeness, Fig. S6† shows the results of SIMS surface profiling for additional gold oxide species.

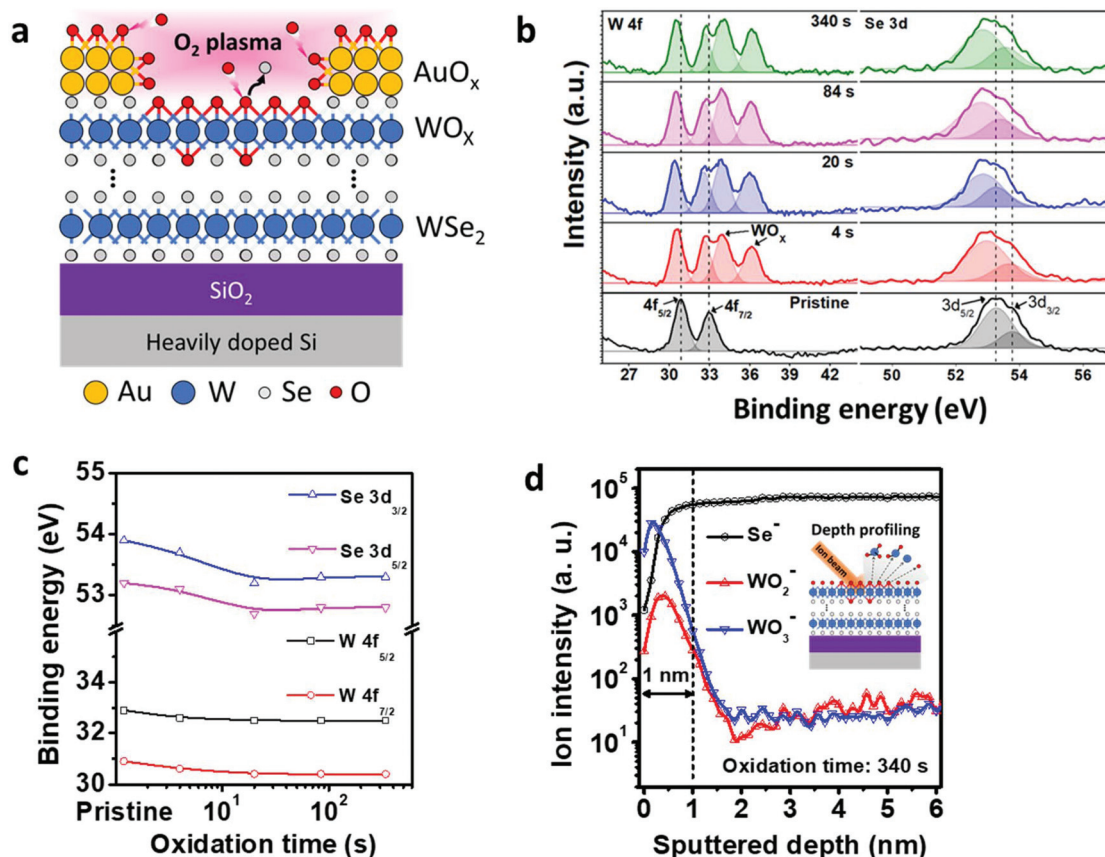


**Fig. 1** Chemical composition of the oxidized  $\text{WSe}_2$  FET. (a) A schematic of the oxidized  $\text{WSe}_2$  FET. Oxygen plasma treatment is performed on the surface of multi-layer  $\text{WSe}_2$  and the gold electrode. (b) XPS results for the oxidized  $\text{WSe}_2$  with respect to the oxidation time. Two new peaks appeared, indicating the existence of  $\text{WO}_x$ . (c) Binding energy shifts of W and Se with oxidation time. As the time increases, the binding energy decreases by about 0.5 eV. (d) SIMS depth profile for the oxidized  $\text{WSe}_2$  at 340 s of plasma oxidation. The selenium ions reduced and tungsten oxide ions ( $\text{WO}_2^-$ ,  $\text{WO}_3^-$ ) increased within 1 nm depth.

### Electrical characteristics of the oxidized $\text{WSe}_2$ FET

In order to assess the impact of plasma oxidation on the electrical characteristics of a device, we fabricated a back-gated FET on multilayer (~7 nm)  $\text{WSe}_2$ . The FET was measured after the initial fabrication and then subsequently after each successive plasma oxidation treatments that were applied to the structure for a cumulative plasma oxidation time of 340 seconds. Four-point probe measurements were used to determine the electrical device characteristics, as shown in Fig. 2a. Fig. 2b shows the optical image of the FET used in this study. The AFM measurement shows that the  $\text{WSe}_2$  thickness does not change even after plasma oxidation.

Fig. 2c shows that the pristine  $\text{WSe}_2$  FET exhibits the dominant n-type ambipolar characteristics. However, after only 4 seconds of plasma oxidation, the electron current decreased by about 20× and the hole current increased by 8×, indicating the dominant p-type ambipolar behavior. After 20 seconds of cumulative plasma oxidation, the dominant p-type FET characteristics were obtained from the transfer characteristics and the hole current at  $V_G = -60$  V rises by ~100× compared to the pristine state. For 340 seconds of cumulative plasma oxidation,

the degenerate p-type characteristics were seen with a hole current of  $4.8 \times 10^{-6}$  A at  $V_G = -60$  V and  $V_{DS} = 0.1$  V. The degenerate p-type doping prevents the effective modulation of the channel carrier concentration by the gate, resulting in a poor on/off ratio of only 6×.

The four point conductance between the V1 and V2 electrodes can be determined from  $G_{4p} = I_D / (V_1 - V_2)$  and the results for all the oxidation times are shown in Fig. S7.† Here,  $I_D$  and  $V_1 - V_2$  values are obtained from the forward sweep of the gate bias. The channel conductance for 340 seconds of oxidation is shown on a linear scale in Fig. 2d. The channel conductance is nearly linear from the range of  $V_G = -60$  to  $-50$  V, which allows us to calculate the field effect mobility for a device biased in the linear regime from the expression

$$\mu_{FE} = \frac{L_{12}}{WC_{OX}} \cdot \frac{dG_{4p}}{dV_G}, \quad (1)$$

where,  $L_{12}$  is the length between the V1 and V2 electrodes, which is equal to 3  $\mu\text{m}$ ,  $W$  is the width of the channel, which is equal to 14  $\mu\text{m}$ , and  $C_{ox}$  is the oxide capacitance of 285 nm of  $\text{SiO}_2$  (equal to  $1.2 \times 10^{-8}$  F  $\text{cm}^{-2}$ ). From the linear regime of

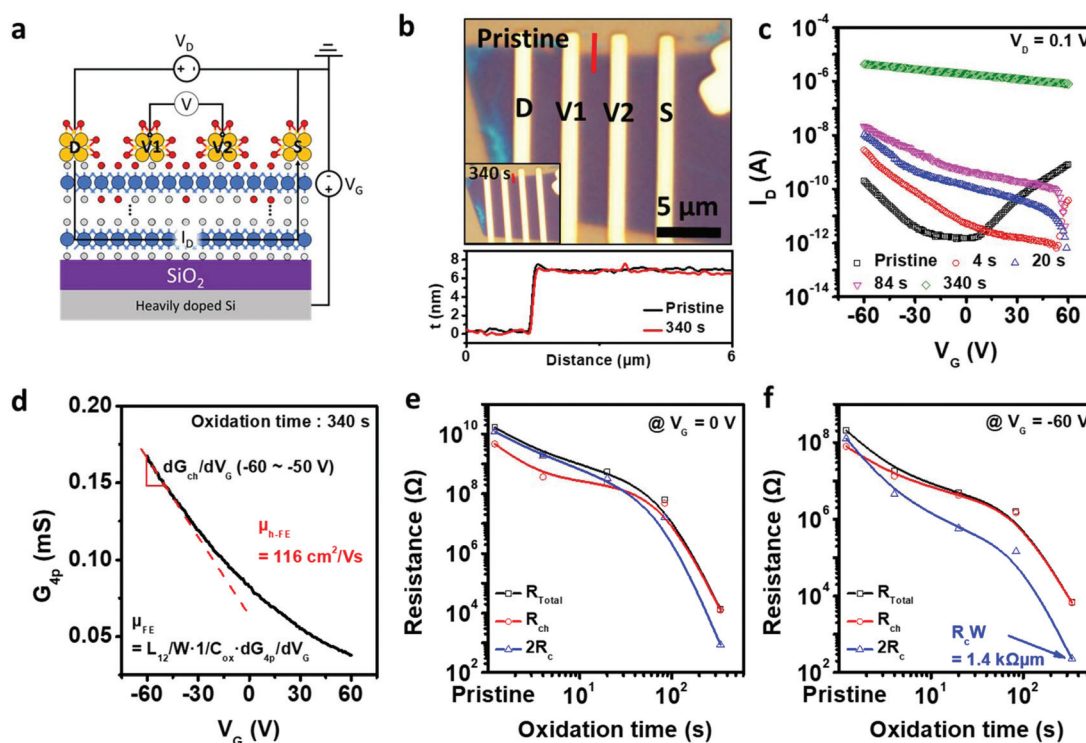


**Fig. 2** Electrical characteristics of oxidized WSe<sub>2</sub> FET. A schematic diagram of four point (drain, source, V<sub>1</sub>, V<sub>2</sub>) structured WSe<sub>2</sub> FET. (b) Optical image of the fabricated FET. The WSe<sub>2</sub> thickness does not change even after plasma oxidation. (c)  $I_D$ – $V_G$  graph @  $V_D = 0.1$  V. As the oxidation time increases, the electron current decreases while the hole current increases. A degenerate p-type state was observed for 340 s of plasma oxidation. (d) 4 point conductance vs. gate bias @ 340 s of plasma oxidation. The maximum field effect mobility is measured to be  $116 \text{ cm}^2 \text{ V}^{-1} \text{ s}^{-1}$ . (e) Resistance vs. oxidation time @  $0 V_G$ . The gate bias had more effect on the contact regions than on the channel. (f) Resistance vs. oxidation time @  $-60 V_G$ . The oxidation has a greater effect on the contact area than on the channel. The minimum normalized contact resistance ( $R_c W$ ) is  $1.4 \text{ k}\Omega \mu\text{m}$  at 340 s.

the curve for the sample after 340 seconds of plasma oxidation, a respectable hole mobility of  $116 \text{ cm}^2 \text{ V}^{-1} \text{ s}^{-1}$  was obtained according to eqn (1).

The channel resistance ( $R_{ch}$ ), contact resistance ( $2R_c$ ), and total resistance ( $R_{total}$ ) of the WSe<sub>2</sub> FET is plotted in Fig. 2e and f. The channel resistance was found from the inverse of the four point conductance and  $2R_c$  was calculated from  $2R_c = R_{total} - R_{ch}$ . As the oxidation time increases, it is clearly displayed that the resistances decrease due to the p-type doping-effect of plasma oxidation.

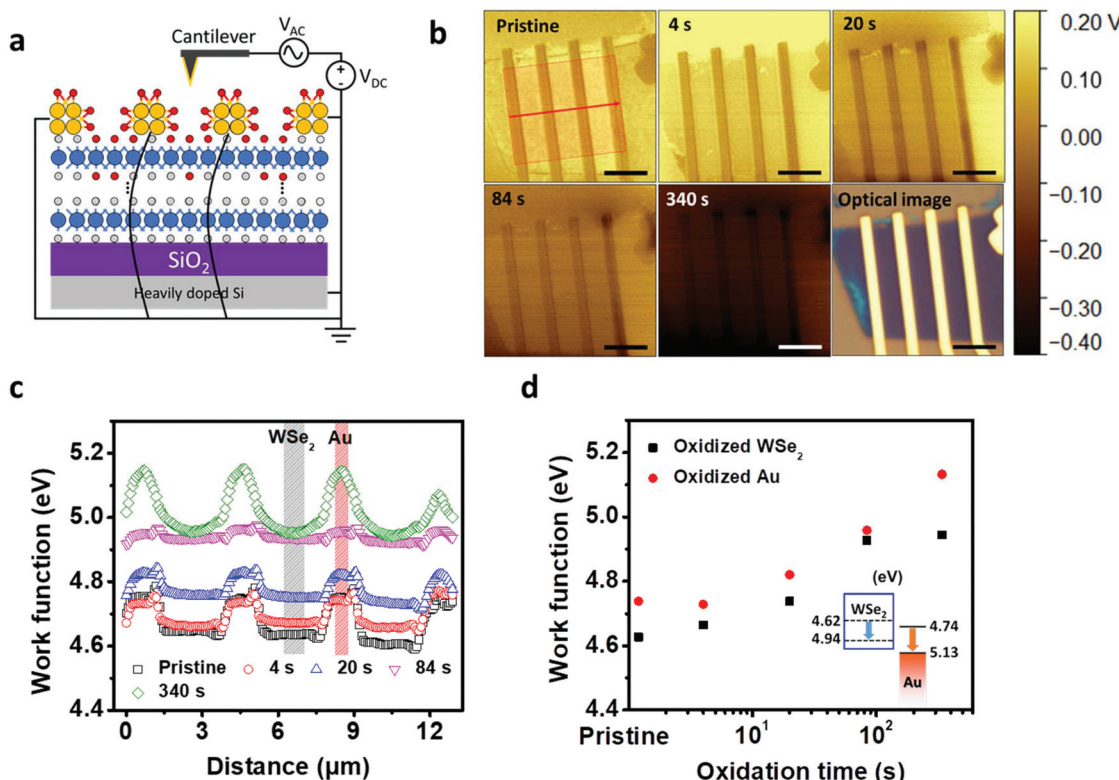
In Fig. 2e, at the pristine state, the device is contact limited as the contact resistance is  $2.5\times$  greater than the channel resistance at  $V_G = 0$  V. However, after 84 seconds of oxidation, the channel resistance drops below the contact resistance. For longer oxidation times, both the resistances drop and after 340 seconds of treatment, the channel resistance is  $15\times$  larger than the contact resistance, thus resulting in a channel dominated device that is desirable for high performance device operation. We confirmed the conversion from the contact-dominated pristine devices to the channel-dominated devices after sufficient oxidation time (with all the resistances dropping with increased oxidation) from the repeated experiments.

In Fig. 2f, the resistance at  $V_G = -60$  V is displayed with respect to the oxidation time. A global back gate bias of  $-60$  V

induces hole carriers in the FET channel and contact region, thereby allowing the hole current to flow dominantly through the channel. Compared with the no gate bias, the channel resistance was reduced by 30 times and the contact resistance was reduced by 230 times on average. It is confirmed that global back gating has more influence on the resistance change of the contact region than the channel region. The minimum contact resistance achieved was  $1.4 \text{ k}\Omega \mu\text{m}$  for a maximum oxidation time of 340 seconds.

#### Local work functions of the oxidized WSe<sub>2</sub> device

Fig. 3 shows the KPFM setup and the measurement results for the local work function as a function of position across the WSe<sub>2</sub> FET. Fig. 3a shows how the FET is biased during a KPFM measurement. First, a cantilever for KPFM with chromium and gold coating on the metal tip surface was used, and AC bias for generating the resonance frequency and DC bias for the potential measurement were applied through the cantilever. During the measurement, the four electrodes of the FET were grounded (details shown in Fig. S8†). Fig. S9† shows that inaccurate surface potentials are measured when proper grounding is not performed since charge accumulates on WSe<sub>2</sub> during measurement and cannot be removed due to the large resistance of the thick insulating layer of SiO<sub>2</sub>.



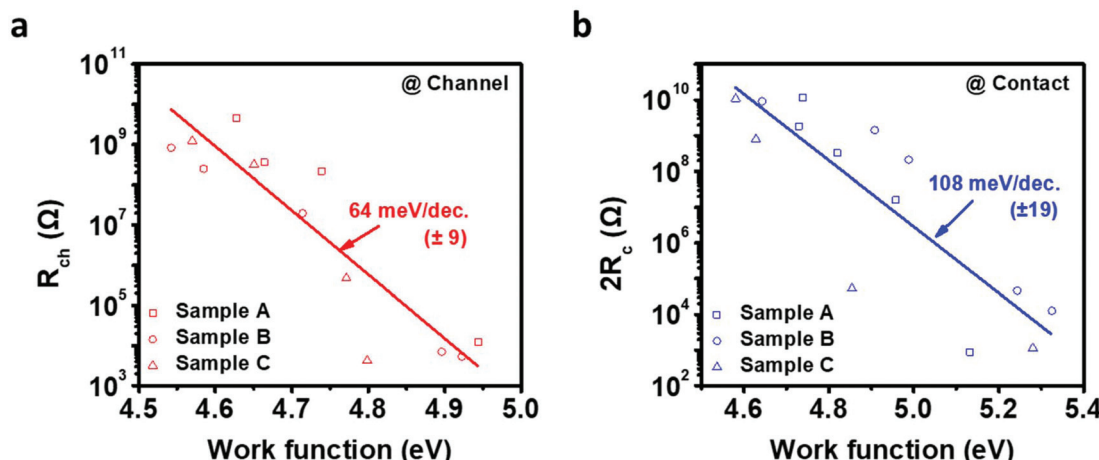
**Fig. 3** Work function of the oxidized WSe<sub>2</sub> channel and the gold electrode measured by KPFM. (a) A schematic of WSe<sub>2</sub> FET under KPFM. All the four electrodes of FET were grounded. (b) Potential mapping of WSe<sub>2</sub> FETs with plasma oxidation time (scale bar: 5 μm). The potential extraction had been done at the red rectangular area (13 × 11 μm). (c) Work functions calculated from the line-extracted potentials. (d) Work function vs. oxidation time. The insets are the band diagrams related to the work function variation. While the work function of WSe<sub>2</sub> increased by 0.3 eV, that of Au increased by 0.4 eV.

Fig. 3b shows the KPFM potential mapping results with respect to oxidation time. To minimize the temporal changes in the effects of plasma treatment, we performed KPFM within 5 minutes after plasma treatment. In the pristine state, the channel region appears bright yellow, indicating a contact potential difference near 0.15 V. However, as the oxidation time increases, the color becomes darker and the contact potential difference for the channel decreases to −0.15 V at 340 seconds. In addition, the potential of the electrode is shown to be always darker than that of WSe<sub>2</sub>. This shows that the work function of the gold electrode is larger than that of the WSe<sub>2</sub> channels. The optical image on the bottom right side is inserted for reference. For quantitative analysis, the potentials were extracted from the area denoted by a red rectangle (13 × 11 μm<sup>2</sup>).

The KPFM scan was performed along the direction of the red arrow, as shown in Fig. 3b, and the value of the contact potential difference (averaged along the direction perpendicular to the scan direction) is plotted in Fig. S10.† The potential of the WSe<sub>2</sub> channel decreased from 153 mV to −163 mV with the increase in the oxidation time. Also, the contact potential difference of the gold electrodes lowered from 41 mV to −352 mV with the increase in the oxidation time. To translate these contact potential differences to work function values, we

need to know the work function of the KPFM metal tip. Accordingly, the contact potential difference of a highly oriented pyrolytic graphite (HOPG) reference sample with a work function of 4.65 eV<sup>25</sup> was measured. To ensure the consistency of our measurements as a function of time, we performed KPFM on the HOPG sample before every KPFM measurement of our sample. The average contact potential difference for the HOPG reference was 140 mV and the standard deviation was 35 mV. Therefore, we determine the work function of the metal tip to be 4.79 eV ( $\phi_{\text{tip}} = \phi_{\text{HOPG}} = +eV_{\text{CPD}}$ ).

Given the work function of the metal tip, we determine the local work function to be  $\phi_{\text{sample}} = 4.79 \text{ eV} - eV_{\text{CPD}}$ , and we obtained the work functions for WSe<sub>2</sub> and Au, as shown in Fig. 3c. The contact potential difference of the channel region continuously decreased with the oxidation time. Interestingly, the contact potential difference of the gold electrode decreased as well. Brown *et al.* explained that the adsorption of the O–O group on the gold surface by oxygen plasma treatment increases the work function by about 0.4–0.5 eV<sup>14</sup> and is confirmed by other works.<sup>11,12,23</sup> Therefore, plasma oxidation not only changes the work function of the WSe<sub>2</sub> channels but also the gold electrodes. However, since KPFM only measures the surface potential, thus, it cannot directly measure the work function of the bottom gold region in direct contact with the



**Fig. 4** Resistance vs. work function. (a) The channel resistance vs. the channel work function @  $V_G = 0$  V. The channel resistance decreases exponentially with increasing channel work function of  $64 (\pm 9)$  meV per dec. It approaches the thermal limit according to the Maxwell-Boltzmann carrier statistics of  $\ln(10) \times kT/q = 60$  mV per dec. (b) The contact resistance vs. the contact work function @  $V_G = 0$  V. The contact resistance decreases exponentially with increasing contact work function of  $108 (\pm 19)$  meV per dec. The contact region increases the work function by about 1.7 times than the channel region for the decade reduction of resistance.

WSe<sub>2</sub> channel. Since the contact area is completely covered with gold, we expect no oxidation at the gold/WSe<sub>2</sub> interface. However, since the transfer length of the TMDC (MoS<sub>2</sub>) FET is only  $\sim 35$  nm at the near edge,<sup>24</sup> it is expected that the oxidized gold is contacted by the oxidized WSe<sub>2</sub> at the edge.

Fig. 3d shows that the work function of WSe<sub>2</sub> was 4.62 eV in the pristine state and increased with plasma treatment time. However, the increase is stagnant after 84 seconds and ends up at 4.94 eV at 340 seconds. From repeated experiments, it is observed that the time for which the increase in WSe<sub>2</sub> work function is stagnant is between 20 seconds (Fig. S12†) and 84 seconds (Fig. S11†). This discrepancy is thought to be caused by the slight non-uniformity of the plasma or the PMMA residues remaining on the WSe<sub>2</sub> surface. It was 4.74 eV in the pristine state of gold and continued to increase to 5.13 eV without stagnation until 340 seconds. The p-type doping of WSe<sub>2</sub> saturated at 84 seconds, while the work function of gold continues to increase so as to enhance the hole carrier transport in the FET. In addition, it was confirmed experimentally that the work function of gold was also stagnant after 340 seconds. In short, the saturation speed of WSe<sub>2</sub> is relatively faster than gold. The band diagrams are shown in the inset for an intuitive understanding of how the work function varies in Au and WSe<sub>2</sub>, from the pristine state to the oxidized state after 340 seconds of oxidation.

#### Relationship between resistance and the work function

Combining the previous results, we plot the channel and contact resistance as a function of the extracted work function in Fig. 4 (as previously discussed, higher work functions correspond to longer oxidation times). We compare the resistance and work functions for three different FETs subjected to the same process conditions and oxidation times (labeled Sample A, B, and C in Fig. 4). Sample A is the device shown in

the previous figures, Sample B is plotted in Fig. S11,† and Sample C is plotted in Fig. S12.†

Fig. 4a shows the relationship between channel resistance and channel work function. The linear fitted red trend line indicates that the channel resistance decreases exponentially with increasing oxidized WSe<sub>2</sub> channel work function. A work function increase of 64 meV (the standard deviation was 9) reduces the channel resistance by  $10\times$  on average, which corresponds well with the theoretical limit of  $\ln(10) \times kT/q = 60$  mV per dec,<sup>4</sup> which is expected from the Maxwell-Boltzmann carrier statistics, thus implying that the oxidized WSe<sub>2</sub> channel is very clean and defect-free.

Fig. 4b shows the relationship between the contact resistance and contact work function. The linear fitted blue trend line indicates that the contact resistance decreased exponentially with increasing oxidized gold contact work function. A work function increase of 108 meV (the standard deviation was 19) reduces the contact resistance by  $10\times$  on average. It implies that the contact region needs to increase the work function by about 1.7 times more than the channel region for the decade resistance reduction. This is expected from the Fermi level pinning generated in the contact region.

### 3. Conclusion

We have shown the formation of tungsten oxide on WSe<sub>2</sub> FETs by using the oxygen plasma treatment. With increased oxidation times, the WSe<sub>2</sub> FET becomes strongly p-type doped from an initial ambipolar state. At the same time, the surface work function increased 0.3 eV at the channel regions and 0.4 eV at the surface of the gold contacts. The best contact resistance achieved was  $1.4 \text{ k}\Omega \mu\text{m}$  for a maximum oxidation time of 340 seconds. The channel resistance was shown to

decrease exponentially with increasing WSe<sub>2</sub> work function. The channel resistance decreases exponentially with increasing channel work function of 64 meV per dec, approaching the thermal limit according to the Maxwell-Boltzmann carrier statistics of  $\ln(10) \times kT/q = 60$  mV per dec and indicating that the oxidized WSe<sub>2</sub> channel is very clean and defect-free. From these measurements and comparisons, we show the controlled p-type doping of a WSe<sub>2</sub> FET by oxygen plasma, which is useful for realizing junctions in future device structures. These methods are also applicable to other types of transition metal dichalcogenide materials, such as MoTe<sub>2</sub>, as shown in Fig. S13.<sup>†</sup>

## 4. Methods

We used XPS and SIMS to analyze the surface of our devices, Kelvin probe force microscopy (KPFM) for work function measurement, and a semiconductor parameter analyzer for *I*-*V* characteristics of the FET devices. Both the *I*-*V* and KPFM measurements were performed on the same FET devices.

### KPFM setup

KPFM consisting of an AFM body (XE-100, Park Systems) and a lock-in amplifier (Park Systems) was designed to apply voltage on the AFM tip. The tip was coated with gold (PPP-NCSTAu, Park Systems) so as to have high conductivity. A voltage of 2 V was applied to the tip through the lock-in amplifier at a frequency of 17.5 kHz. The metallic sample chuck was connected to the ground of the equipment. The AFM body was placed in an electric field shielding box, which was maintained at room temperature with atmospheric pressure and dehumidification conditions (<25%).

### Oxygen plasma treatment (p-type doping of WSe<sub>2</sub>)

Oxygen plasma was used to treat WSe<sub>2</sub> to create a p-type semiconductor. The plasma source was designed to generate inductively coupled plasma (ICP), which was operated at a RF of 13.56 MHz, a power of 20 W, a base pressure of  $8.0 \times 10^{-6}$  Torr, and a working pressure of 30 mTorr. The plasma treatment time varied from 0 to 340 s. No additional treatment was done during the plasma treatment.

### X-ray photoemission microscopy measurement

The XPS sample was prepared by exfoliating the bulk WSe<sub>2</sub> materials on 285 nm thick SiO<sub>2</sub> deposited on a silicon wafer at a size of 0.5 cm × 0.5 cm using mechanical exfoliation method, while the material covered up to 70% of the substrate. The XPS equipment (MultiLab 2000, Thermo VG) used a Mg K $\alpha$  source. It was operated at an ultrahigh vacuum of  $10^{-11}$  Torr. The measured XPS peaks were calibrated based on the C 1s peak (284.5 eV).

### Device fabrication for field effect transistor:

We prepared few-layered WSe<sub>2</sub> and MoTe<sub>2</sub> on a SiO<sub>2</sub> substrate in the same way as the previous KPFM sample by coating the

sample using PMMA A4 495 (Microchem) at a speed exceeding 4000 rpm for 60 s and annealing it over 180 °C for 90 s. The PMMA A6 950 (Microchem) was also coated with the same recipe as that used for PMMA A4. The device electrode patterns were prepared by electron beam lithography (EBL). After the EBL process, the sample was developed using a solution consisting of IPA : DI water = 3 : 1 at 4 °C. It was then rinsed with IPA for 30 s and dried by N<sub>2</sub> gas blowing. The next step was gold deposition by electron beam deposition (EBD) to form metal electrodes of FET. EBD was performed at a base pressure of  $5 \times 10^{-8}$  Torr, a working pressure of  $2 \times 10^{-7}$  Torr, and a deposition speed of 1 Å s<sup>-1</sup>. These samples were treated in acetone for 1.5 hours for the lift-off process, rinsed for 30 s with IPA, and blown by N<sub>2</sub> gas. FET size having a channel length of 3 μm and an electrode length of 1 μm was uniformly prepared. An Agilent 4155C semiconductor analyzer and a probe station (M6VC, MSTECH) were used to measure the  $I_D$ - $V_G$  characteristics (transfer curve).

### Secondary ion mass spectroscopy (SIMS) depth profiling mode

The SIMS sample was prepared by exfoliating TMDC materials with a bulky and large size (~200 μm) on 285 nm thick SiO<sub>2</sub> deposited on a silicon wafer with a size of 1 cm × 1 cm. The SIMS equipment (TOF SIMS 5, ion TOF) used a Cs<sup>-</sup> source. The beam diameter was 20 μm and the beam power was 10 nA. It was operated at an ultrahigh vacuum of  $10^{-10}$  Torr. The measured SIMS ion intensity was calibrated based on the carbon ion peak.

### Secondary ion mass spectroscopy (SIMS) surface profiling mode

The SIMS sample was prepared by depositing 50 nm gold on 500 μm thick Si wafer with a size of 1 cm × 1 cm. The SIMS equipment (TOF SIMS 5, ion TOF) used a Bi<sup>-</sup> source. The beam diameter was 300 μm × 300 μm and the beam dose was  $8.06 \times 10^8$ . The depth up to which effect of the ion beam is present was considered to be up to three atomic layers. It was operated at an ultrahigh vacuum of  $10^{-10}$  Torr. The measured SIMS ion intensity was calibrated based on the carbon ion peak.

## Author contributions

I. Moon, S. Lee, M. Lee, and C. Kim have conducted the materials' preparation, device fabrication, and measurements of the materials and electrical properties under the supervision of W. J. Yoo. D. Seol and Y. Kim conducted the surface measurements and analysis. K. H. Kim and Y. G. Yeom conducted the plasma etching processes. I. Moon, S. Lee, J. Teherani, J. Hone, and W. J. Yoo participated in the preparation of the manuscript.

## Conflicts of interest

There are no conflicts to declare.

## Acknowledgements

This work was supported by the National Research Foundation of Korea (NRF) as the Basic Science Research Program (2018R1D1A1B07044712), the Global Research Laboratory (GRL) Program (2016K1A1A2912707) and the Global Frontier R&D Program (2013M3A6B1078873).

## References

- 1 K. S. Novoselov, A. K. Geim, S. V. Morozov, D. A. Jiang, Y. Zhang, S. V. Dubonos, I. V. Grigorieva and A. A. Firsov, *Science*, 2004, **306**, 666.
- 2 F. Xia, H. Wang, D. Xiao, M. Dubey and A. Ramasubramaniam, *Nat. Photonics*, 2014, **8**, 899.
- 3 J. Gusakova, *et al.*, *Phys. Status Solidi A*, 2017, **214**, 1700218.
- 4 H. Fang, S. Chuang, T. C. Chang, K. Takei, T. Takahashi and A. Javey, *Nano Lett.*, 2012, **12**, 3788.
- 5 J. Kang, S. Tongay, J. Zhou, J. Li and J. Wu, *Appl. Phys. Lett.*, 2013, **102**, 22.
- 6 J. Meyer, S. Hamwi, M. Kröger, W. Kowalsky, T. Riedl and A. Kahn, *Adv. Mater.*, 2012, **24**, 5408.
- 7 F. Ahmed, Y. D. Kim, M. S. Choi, X. Liu, D. Qu, Z. Yang, J. Hu, I. P. Herman, J. Hone and W. J. Yoo, *Adv. Funct. Mater.*, 2017, **27**, 1.
- 8 P. Zhao, D. Kiriya, A. Azcatl, C. Zhang, M. Tosun, Y.-S. Liu, M. Hettick, J. S. Kang, S. McDonnell, S. KC, J. Guo, K. Cho, R. M. Wallace and A. Javey, *ACS Nano*, 2014, **8**, 10808.
- 9 M. Yamamoto, S. Nakaharai, K. Ueno and K. Tsukagoshi, *Nano Lett.*, 2016, **16**, 2720.
- 10 M. Yamamoto, S. Dutta, S. Aikawa, S. Nakaharai, K. Wakabayashi, M. S. Fuhrer, K. Ueno and K. Tsukagoshi, *Nano Lett.*, 2015, **15**, 2067.
- 11 M. W. A. Hou, C. R. M. Gazoni and R. J. Reeves, *Appl. Phys. Lett.*, 2019, **33** 502, 1.
- 12 L. Fu, N. Q. Wu, J. H. Yang, F. Qu, D. L. Johnson, M. C. Kung, H. H. Kung and V. P. Dravid, *J. Phys. Chem. B*, 2005, **109**, 3704.
- 13 J. Sylvestre, S. Poulin, A. V. Kabashin, E. Sacher, M. Meunier and J. H. T. Luong, *J. Phys. Chem. B*, 2004, **108**, 16864.
- 14 T. M. Brown, G. M. Lazzerini, L. J. Parrott, V. Bodrozic, L. Bürgi and F. Cacialli, *Org. Electron.*, 2011, **12**, 623.
- 15 S. Y. Lee, U. J. Kim, J. Chung, H. Nam, H. Y. Jeong, G. H. Han, H. Kim, H. M. Oh, H. Lee, H. Kim, Y. G. Roh, J. Kim, S. W. Hwang, Y. Park and Y. H. Lee, *ACS Nano*, 2016, **10**, 6100.
- 16 D. Xiang, C. Han, J. Wu, S. Zhong, Y. Liu, J. Lin, X.-A. Zhang, W. P. Hu, B. Özyilmaz, A. H. C. Neto, A. T. S. Wee and W. Chen, *Nat. Commun.*, 2015, **6**, 6485.
- 17 Y. Almadori, N. Bendiab and B. Grévin, *ACS Appl. Mater. Interfaces*, 2018, **10**, 1363.
- 18 Y. Feng, K. Zhang, H. Li, F. Wang, B. Zhou, M. Fang, W. Wang, J. Wei and H. S. P. Wong, *Nanotechnology*, 2017, **28**, 295705.
- 19 F. Fuchs, F. Caffy, R. Demadrille, T. Mélin and B. Grévin, *ACS Nano*, 2016, **10**, 739.
- 20 D. Qu, X. Liu, M. Huang, C. Lee, F. Ahmed, H. Kim, R. S. Ruoff, J. Hone and W. J. Yoo, *Adv. Mater.*, 2017, **29**, 1.
- 21 S. R. Das, K. Wakabayashi, M. Yamamoto and K. Tsukagoshi, *J. Phys. Chem. C*, 2018, **122**, 17001.
- 22 Y. Ping and G. Galli, *J. Phys. Chem. C*, 2014, **118**, 6019.
- 23 B. M. G. Helander, Z. Wang, M. T. Greiner, Z. Liu, J. Qiu and Z. Lu, *Adv. Mater.*, 2010, **22**, 2037.
- 24 C. D. English, G. Shine, V. E. Dorgan, K. C. Saraswat and E. Pop, *Nano Lett.*, 2016, **16**, 3824.
- 25 O. Ochedowski, G. Begall, N. Scheuschner, M. El Kharrazi, J. Maultzsch and M. Schleberger, *Nanotechnology*, 2012, **23**, 405708.